PNAS RESEARCH ARTICLE | APPLIED PHYSICAL SCIENCES

Stress accumulation by confined ice in a temperature gradient

Dominic Gerber[a], Lawrence A. Wilen[b], Florian Poydenot[c], Eric R. Dufresne[a], and Robert W. Style[a,1]

Edited by Sharon Glotzer, University of Michigan, Ann Arbor, MI; received January 14, 2022; accepted May 20, 2022

When materials freeze, they often undergo damage due to ice growth. Although this damage is commonly ascribed to the volumetric expansion of water upon freezing, it is usually driven by the flow of water toward growing ice crystals that feeds their growth. The freezing of this additional water can cause a large buildup of stress. Here, we demonstrate a technique for characterizing this stress buildup with unprecedented spatial resolution. We create a stable ice–water interface in a controlled temperature gradient and measure the deformation of the confining boundary. Analysis of the deformation field reveals stresses applied to the boundary with $\mathcal{O}$(micrometers) spatial resolution. Globally, stresses increase steadily over time as liquid water is transported to more deeply undercooled regions. Locally, stresses increase until ice growth is stalled by the confining stresses. Importantly, we find a strong localization of stresses, which significantly increases the likelihood of damage caused by the presence of ice, even in apparently benign freezing situations. Ultimately, the limiting stress that the ice exerts is proportional to the local undercooling, in accordance with the Clapeyron equation, which describes the equilibrium between a stressed solid and its melt. Our results are closely connected to the condensation pressure during liquid–liquid phase separation and the crystallization pressure for growing crystals. Thus, they are highly relevant in fields ranging from cryopreservation and frost heave to food science, rock weathering, and art conservation.

freezing | premelting | frost heave | crystallization pressure

Significance

Ice almost always causes damage when soft, wet materials freeze. This poses a tremendous, unsolved challenge across a huge variety of scientific disciplines. This damage is not typically caused by freezing water expanding but by the process of cryosuction—which continues after ice's initial growth. Here, we characterize how stresses build up in this process with unprecedented microscale resolution. Our technique shows how stresses are extremely localized and with great damage potential. Stresses globally increase while locally stalling at a value that is set by the local undercooling. Beyond freezing, our work allows us to measure local disjoining pressures with micrometer-scale resolution and has strong ties with the science of confined crystal growth, such as in salt weathering.

We all know that when water freezes, its volume increases by about 9%. While this explains how a filled water bottle cracks in a freezer, it does not explain the huge deformations underlying freezing damage to roads (i.e., frost heave), food, or biological tissue (1). These more dramatic effects typically occur in a temperature gradient and are associated with a flux of liquid water into regions below freezing called cryosuction.

Ice grows due to cryosuction via the transport of water along undercooled liquid films that surround the ice. These films can exist at boundaries between ice and its confining material. There, interfacial forces combine to give a repulsive interaction between the ice and the surrounding substrate, which results in a nanoscopic, intervening layer of liquid water between the two materials (Fig. 1) (2–8). Bulk water can also exist in small pores of frozen porous materials or at corners of ice crystals. In that case, the ice–water interface becomes highly curved, and the surface tension of this interface results in a local reduction of the freezing temperature—described by the Gibbs–Thomson equation (9–11).

Flow in this premelted liquid can be driven by either temperature gradients or gradients of stress in the ice. A complete description is given by nonequilibrium thermodynamics (12, 13). However, we can capture the essential features of the flow by considering the implications of thermodynamic equilibrium between ice and the undercooled water immediately adjacent to it. This local equilibrium is expressed by the Clapeyron equation:

$$-\sigma_{nn}^{ice} - P_l = \rho q_m \frac{T_m - T}{T_m}. \quad [1]$$

Here, ρ is the ice density, T_m is the bulk freezing temperature at atmospheric pressure, q_m is the latent heat of melting, and σ_{nn}^{ice} is the normal stress exerted by the ice on the substrate. P_l is the hydrodynamic pressure of the liquid, defined as the pressure of a bulk reservoir of water that would be in thermodynamic equilibrium with the liquid directly adjacent to the ice. To avoid confusion, we note that P_l differs from the local pressure in the liquid, P_l^f (the latter is also commonly used in the freezing literature, and $P_l^f = P_l + \Pi$, where Π is the local disjoining pressure in the premelted liquid layer). Liquid flow arises due to gradients in P_l (1). Thus, we see that that flow can be caused either by gradients in σ_{nn}^{ice} or by temperature gradients. Note that Eq. **1** makes several underlying assumptions, such as ignoring density differences between ice and water (1, 9, 14). These assumptions are detailed in *SI Appendix*.

A specific example demonstrating how flow in premelted films causes stresses to build up is shown in Fig. 1. Here, ice is formed in a static temperature gradient, ∇T.

Author affiliations: [a]Department of Materials, ETH Zürich, 8093 Zürich, Switzerland; [b]Center for Engineering Innovation and Design, School of Engineering and Applied Sciences, Yale University, New Haven, CT 06520; and [c]Laboratoire de Physique de l'École Normale Supérieure, UMR8023, CNRS, Université de Paris, Paris Sciences et Lettres Research University, 75005 Paris, France

Author contributions: D.G., L.A.W., F.P., E.R.D., and R.W.S. designed research; D.G. and F.P. performed research; D.G., L.A.W., E.R.D., and R.W.S. analyzed data; and D.G., E.R.D., and R.W.S. wrote the paper.

The authors declare no competing interest.

This article is a PNAS Direct Submission.

[1]To whom correspondence may be addressed. Email: robert.style@mat.ethz.ch.

This article contains supporting information online at https://www.pnas.org/lookup/suppl/doi:10.1073/pnas.2200748119/-/DCSupplemental.

Published July 29, 2022.

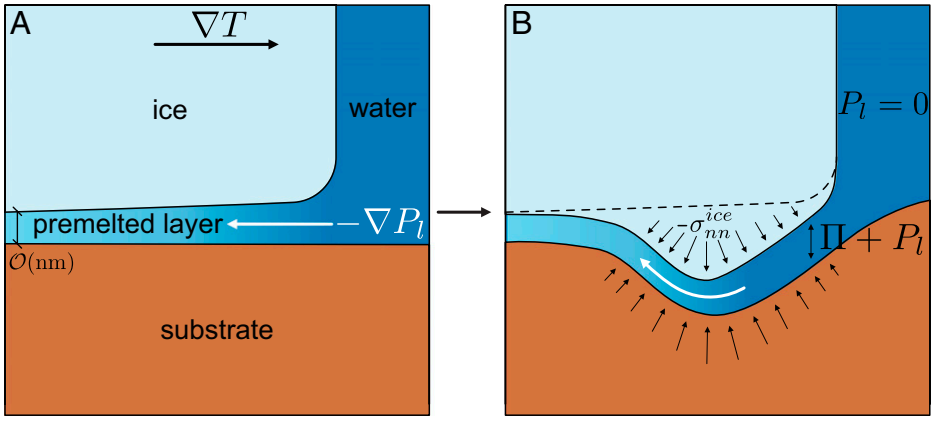

Fig. 1. Schematic showing how stresses build up due to cryosuction in a temperature gradient. (*A*) Initially, both ice and substrate are stress free. (*B*) Cryosuction causes ice accretion and stress buildup near the bulk ice–water interface.

Assuming that the ice is initially stress free, Eq. **1** implies that $\nabla P_l \sim \nabla T$, causing a flow into and along the premelted layer. As the water moves to colder temperatures, it freezes onto the ice, leading to growth of ice as shown in Fig. 1*B*. This growth deforms the confining boundary and creates stresses that can ultimately damage it.

These theoretical concepts form the basis of cryosuction theory (9, 15–18) and frost heaving (12–14, 19–22). However, they have almost exclusively been tested via macroscale experiments, which measure spatially averaged stresses and ice segregation in porous materials without microscale resolution or without temperature gradients (10, 23–30).

Here, we directly measure the evolving stresses exerted by individual ice crystals in a steady temperature gradient with unprecedented spatial resolution. We grow ice into a soft-walled chamber (31) and monitor the wall deformations, allowing us to measure evolving ice stresses. Locally, stresses increase until they stall at a fixed value. Globally, stresses continuously accumulate over increasingly large areas of the ice–substrate interface.

Our experimental freezing setup, an extension of ref. 32, is shown schematically in Fig. 2*A*. The freezing cell consists of two glass coverslips with a 600-μm spacing, where the bottom coverslip is coated with a thin layer of silicone (33, 34). The layer thickness, h, is adjusted in the range of 88 to 105 μm, and Young's modulus, $E = 22$ to 295 kPa (characterized following ref. 35). To visualize deformations, 200-nm-diameter fluorescent tracer particles are attached to the silicone gel surface, following the protocol in ref. 36, with an average spacing of 10 μm. The freezing cell is mounted on the bottom of two aluminum blocks whose temperature is fixed with a precision of $\pm$ 0.05 °C, allowing us to impose a steady temperature gradient across the cell. With this setup, the ice–water interface position fluctuates by less than 5 μm in experiments lasting up to 6 h. The exact value of ∇T is measured by placing a thermistor in the cell and measuring its distance to the ice–water interface. A 2-mm gap between the blocks lets us image ice growth with bright-field, polarized light, and confocal microscopy (37, 38). *SI Appendix* has further details.

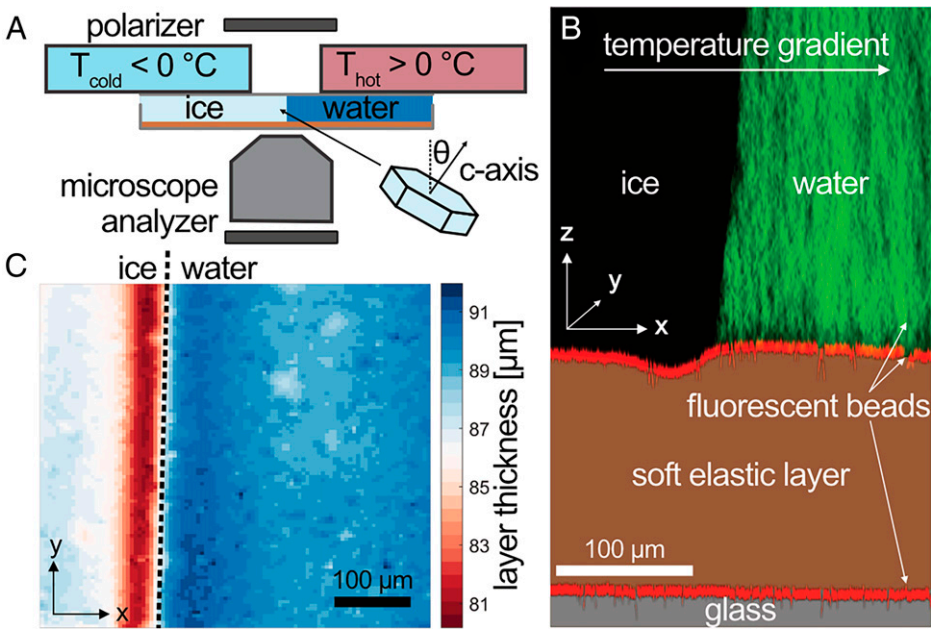

Fig. 2. Imaging substrate deformations in a freezing cell. (*A*) A schematic of the experimental setup showing the angle θ between the *c* axis of the ice crystal and the *z* axis. (*B*) Pseudocolored confocal microscopy image showing a side view of the ice–water interface and the growing indentation into the soft elastic layer below it. The color in the water comes from fluorescent nanoparticles, which are expelled by the growing ice. (*C*) A typical surface profile underneath an ice crystal. The profile is uniform along the ice–water interface, allowing us to collapse the data along it.

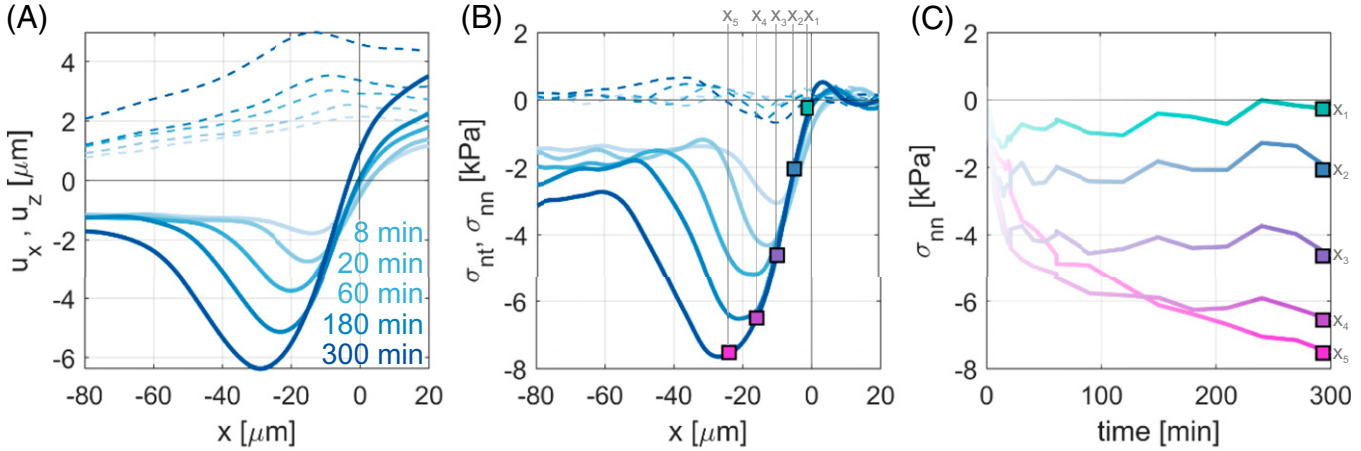

Fig. 3. The time evolution of surface displacements and stresses near an ice–water interface at $x = 0$ (with $E = 22$ kPa, $\nabla T = 0.4$ K/mm, and thickness of 88 μm) for (*A*) substrate displacements u_x (dashed curves) and u_z (continuous curves). (*B*) The corresponding traction and normal stresses σ_{nt} (dashed curves) and σ_{nn} (continuous curves). Lower (darker) curves are at later times. (*C*) Evolution of σ_{nn} over time at the x positions marked in *B*.

To perform the experiment, we fill a cell with deionized water that has been allowed to equilibrate with the room atmosphere [i.e., it contains a small amount of dissolved air (39)]. We also add a minimal amount of fluorescent 100-nm-diameter particles to visualize the ice–water interface (Fig. 2*B*). The cell is cooled to -0.5 °C on one side, and ice is nucleated by touching the cell briefly with a liquid nitrogen–soaked cotton swab. The temperature is slowly reduced (at 0.1 K/min) to grow ice to the edge of the intended imaging region. Then, after 15 min of equilibration time, we start taking confocal stacks and bright-field images. The experiment starts ($t = 0$) at the point when we apply one last small cooling step, advancing the ice into an initially stress-free region. In this way, we are able to capture the very beginning of the stress buildup. The process creates large individual crystals, so that our entire imaging region consists of a single ice crystal (40, 41). We measure its orientation by looking at the crystal color between crossed polarizers (42–45) (*SI Appendix*). This allows us to measure the angle, θ, between the c axis of the ice crystal and the z axis with about 10° accuracy. If the ice exerts stresses on the surrounding cell, we see this as deformations of the silicone layer. We quantify this by measuring the positions of the individual tracer particles with a confocal microscope and tracking their displacements with a resolution of 0.06 μm in the x and y directions and 0.1 μm in the z direction, with x, y, z defined in Fig. 2*B*.

Since the cell is open to atmospheric pressure at both ends, there is no pressure buildup due to water expanding as it freezes. However, stresses still build up next to the ice–water interface due to cryosuction. This can be seen in the raw microscopy data in Fig. 2*C*, where there is a clear indentation in the soft elastic layer next to the ice–water interface. For single crystals, this deformation is always very uniform along the ice–water interface, as shown in Fig. 2*C*, and thus, we average it along the axis of the ice–water–substrate contact line to give two-dimensional representations of the substrate indentations, as shown in Figs. 2*B*, 3, and 4.

A typical example of the evolution of substrate deformations under the ice is shown in Fig. 3*A*. This shows measured horizontal and vertical displacements of the surface (u_x and u_z, respectively) at selected time points. At each time point, these are plotted relative to the position of the ice–water contact line on the substrate. At time 0, the final cooling step is applied to advance the ice. The ice takes ∼10 min to stabilize at its final position, and there is a small amount of substrate deformation during this time. However, after this, we see much larger deformations appear with a continuously growing dimple emerging behind the ice front. Simultaneously, the substrate bulges up on the liquid side of the contact line due to its incompressibility. Initially, the dimple grows quickly but later, slows down significantly (note the growing time intervals). As the indentation grows, its position of maximum indentation also moves to colder temperatures, resulting in a significant volume of ice pushing down into the underlying substrate.

For further insight, we calculate the stresses exerted by the ice with traction force microscopy (TFM) (36, 46). This involves solving a linear-elastic problem to calculate the in- and out-of-plane traction stresses exerted on the silicone surface (σ_{xz} and σ_{zz}, respectively) from u_x and u_z (47). In brief, point values of u_x and u_z are interpolated onto a grid and smoothed to reduce measurement noise. These fields are Fourier transformed and multiplied by a wavelength-dependent kernel function, $Q(E, \nu, h)$, where ν and h are the substrate's Poisson ratio and thickness, respectively. We obtain traction stresses by inverse Fourier transforming and subtracting a uniform value from σ_{zz} to ensure that the average traction stresses on the water side of the interface are zero. This last one is necessary to give absolute values of σ_{zz} when using incompressible substrates but not when calculating σ_{xz} (47). Finally, we rotate these stresses to get σ_{nn} and σ_{nt}, the normal and shear stresses relative to the local substrate surface, respectively. $\sigma_{zz} = \sigma_{nn}$ to excellent approximation, but there is a small quantitative difference between σ_{nt} and σ_{xz}. Further details are given in *SI Appendix*.

The TFM results show that the stresses build up near the contact line, similarly to the substrate deformations (Fig. 3*B*). However, unlike the indentation, both sets of stresses under the water-filled part of the cell are flat and close to zero. This makes sense because the cell is open to the atmosphere, and there is no pressure in the liquid phase. Furthermore, the tangential traction stresses are approximately an order of magnitude smaller than the normal stresses, and the measured horizontal deformations u_x are predominantly caused by the normal stresses. This fits with the schematic picture in Fig. 1 of a lubricated interface between the silicone and the ice.

While the global maximum stress steadily increases, the stress at each position appears to eventually saturate. In Fig. 3*C*, we plot σ_{nn} vs. time at fixed positions behind the ice–water interface. We see that the stresses close to the ice–water interface plateau, suggesting the presence of a local maximum pressure that the ice can exert on its surroundings. The farther away from the interface, the longer it takes for the stress to stall. At the farthest point from the interface shown (pink curve in Fig. 3*C*), the stress buildup

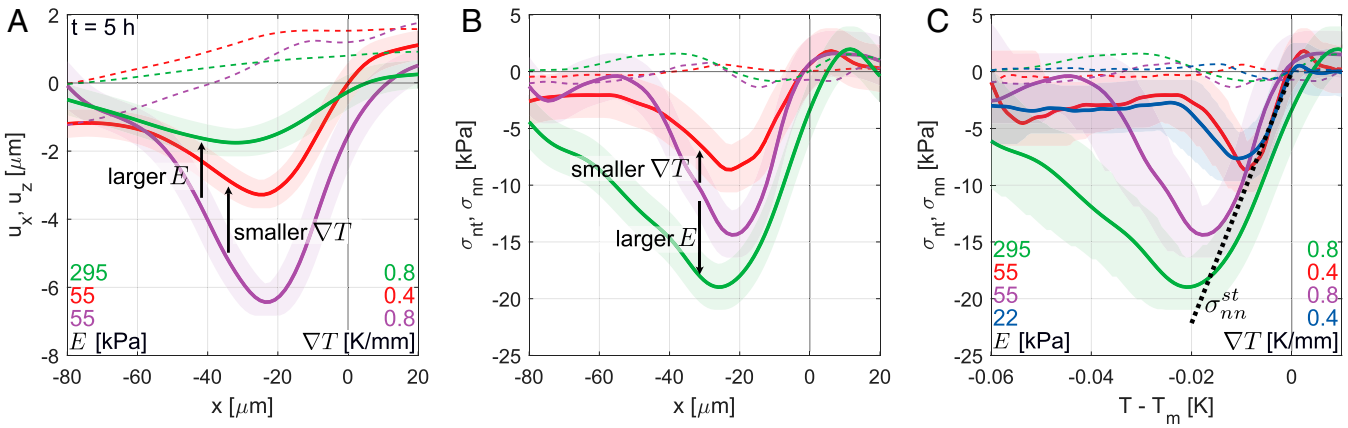

Fig. 4. The effect of E and ∇T on ice growth and stress buildup. (*A*) Substrate displacements u_x (dashed curves) and u_z (continuous curves) for four experiments with different applied temperature gradients and substrate stiffnesses as indicated. The ice–water interface is at $x = 0$. (*B*) The corresponding stresses σ_{nt} (dashed curves) and σ_{nn} (continuous curves). The shaded areas denote experimental uncertainties. *C* shows the same stresses as a function of the local temperature. The dashed line shows the expected stalling stress from Eq. **1**. In all panels, soft, elastic–layer thicknesses are 88, 105, 105, and 88 μm, while crystal orientations are $\theta = 30° \pm 10°$, $82° \pm 8°$, $82° \pm 8°$, and $82° \pm 8°$ for green, red, purple, and blue curves, respectively. The blue curves correspond to the data in Fig. 3.

slows but does not plateau over the course of the experiment. For points close to the interface, there appears to be a small but steady increase in the plateau region. We believe that this is caused by a small drift of the ice–water interface position over the course of the experiment (*SI Appendix*).

We see similar results when we vary ∇T and E. Fig. 4*A* shows the indentation at the same time point for three experiments with similar substrate thickness. Increasing stiffness results in smaller indentations (compare green and purple curves), while increasing the temperature gradient results in a faster ice buildup (compare red and purple curves). Fig. 4*B* shows the calculated stresses corresponding to the data in Fig. 4*A*. As before, there are always negligible shear stresses, and the normal stresses locally stall near the ice–water interface (*SI Appendix*). Interestingly, while the size of the indentation is very sensitive to substrate stiffness, the stresses are much less so. Here, the stresses near the ice–water interface are very comparable for the two experiments with the same temperature gradient, despite a factor of six in stiffness. On the other hand, increasing the temperature gradient by a factor of two seems to approximately double σ_{nn} near the ice–water interface. These results hint at a stall pressure that mainly depends on local temperature.

A local temperature-dependent stall pressure fits remarkably well with the predictions of Eq. **1**, setting $\sigma_{nn}^{ice} = \sigma_{nn}$. Stall should occur when flow from the bulk water into the premelted layer ceases: when $P_l = 0$. This corresponds to a predicted stall stress of $\sigma_{nn}^{st} = -\rho q_m \frac{T_m - T}{T_m}$ [note that a very similar result can also be derived from nonequilibrium thermodynamics (13)]. In Fig. 4*C*, we plot the measured stresses as a function of T, along with the theoretical prediction (dashed line). We see that the measured stall stresses collapse onto a single line that matches the theory to within error bars. This collapse seems to not be affected by ice-crystal orientation. However, it is likely that the stalling dynamics will depend upon θ, as different ice facets have very different premelted-layer thicknesses (6, 48, 49). It is also intriguing that the theory works so well, as it validates the series of assumptions it is based upon (see *SI Appendix*).

While the details of the final local stall pressure only depend on ∇T, the global growth dynamics are more complex. Fig. 4*A* shows that displacements build up fastest in higher temperature gradients and on softer substrates. By contrast, Fig. 4*B* shows that stresses appear to build up fastest in steeper temperature gradients but on stiffer substrates. The distinction between these is important, as it is the stresses that dictate when damage is likely to occur. Ultimately, assuming that ice buildup is fed by flow in premelted films, the dynamics are controlled by the interplay between the hydrodynamic pressure gradients that drive flow and the changes in film thickness that lead to reduced liquid mobility at colder temperatures. This has been modeled for the case of a simple spring-like substrate (9, 17), and our results are in qualitative agreement with that work.

Although it is beyond the scope of this paper, we note that there are two further factors that may alter the dynamics of stress buildup. First, ice growth may not only be fed by flow in premelted films. Silicone is known to be permeable to water, even though water barely swells it (50). Thus, ice could also grow by transport through the bulk of the substrate. Second, premelted film thicknesses are expected to be $\mathcal{O}$(micrometers) thick near the ice–water interface (i.e., much larger than the nanometric films that are caused by interfacial forces alone). This is because the surface energy of the ice–water interface, γ, rounds out the corner of the ice crystal at the three-phase contact line. This rounding causes an effective divergence in the thickness of the premelted film over a distance $L_c = \sqrt{\gamma T_m / \rho q_m G}$ from the contact line (51). In our experiments, $L_c \sim 10$ μm, which is comparable with the length scale over which we see the greatest stress buildups. Thus, it could be that capillarity plays an important role in controlling ice-growth dynamics via the enhanced liquid mobility in this region.

In conclusion, we have characterized how stresses build up around an ice crystal in a steady temperature gradient. Our technique allows us to measure local stresses with $\mathcal{O}$(micrometers) spatial resolution. Near the ice–water front, ice grows by cryosuction, causing normal stresses of $\mathcal{O}$(kPa) to build up within a few minutes. At the same time, ice exerts much smaller shear stresses on its surroundings, presumably because of the lubricating effect of premelted layers between the ice and substrate. Ultimately, the normal stresses reach a stall value of about 1 MPa/K, which is in remarkably good agreement with the long-standing predictions of the Clapeyron equation. This gives strong support to this equation's widespread use as a foundation of freezing theory and in other systems where premelting is important, including glacier movements (52), and alloys and metals at high temperatures (53, 54). Our results show how stress buildup is highly localized,

explaining the large propensity for damage during freezing. This is important for processes like food storage and cryopreservation. We anticipate that our technique can be used to gain insights into the role of additives, like antifreeze proteins and cryopreservants, in protecting against damage. Our work is also closely related to the condensation pressure in liquid–liquid phase separation (55) and to the crystallization pressure observed when crystals form in confinement (56–58), which controls processes ranging from weathering (59) to vein formation in rocks (60). In these cases, pressures caused by supersaturation result in a stress buildup, and our technique offers a simple way to study this.

There is clearly still work to be done to understand the cryosuction process. Here, it takes a relatively long time to build up micrometer-sized deformations with accompanying stresses of $\mathcal{O}(10\,\mathrm{kPa})$. However, in practice, materials can fail even after one short freezing cycle and with smaller temperature gradients. This indicates that faster transport mechanisms are likely present than the premelted film flows that dominate here. One potential mechanism is the flow of supercooled water through porous substrates, like hydrogels or biological tissue. Alternatively, water normally contains significant amounts of solutes, and this is known to strongly influence both bulk freezing (61), and premelted-layer characteristics (62). We hope to address this question in future work.

Materials and Methods

To create the experimental cell, we glued together two glass microscope slides, one of which was coated in a layer of silicone elastomer. The silicone consisted of either Sylgard 184 (Dow Corning) or a mixture of HMS-301 and DMS-V31 with Karstedt's catalyst [Gelest (33)]. The silicone was spin coated onto the glass to give a layer thickness between 85 and 105 μm. After the silicone was cured, the cell was assembled with spacers to give an interior volume that had approximate dimensions of $3 \times 1.5 \times 0.6$ mm. To visualize the glass–silicone interface and the upper surface of the silicone, we attached fluorescent nanoparticles to these interfaces (200-nm carboxylate-modified Fluospheres; Thermo Fisher Scientific) following previous protocols (47).

To image the cell, we filled it with deionized water, attached it to our freezing apparatus with thermal paste, and grew ice by cooling down one side of the cell. The whole freezing apparatus fits on a piezo stage of a confocal microscope (Nikon Ti-2 with a CSU-W1 spinning disk confocal attachment from 3i). We imaged the fluorescent nanoparticles in the sample at regular intervals by taking confocal image stacks with a Nikon 20× air objective (numerical aperture 0.45). This objective was temperature stabilized with a heating collar (TC-HLS-025; Bioscience Tools) to minimize temperature fluctuations in the cell. We processed the images following ref. 47 to obtain the three-dimensional locations of all the fluorescent nanoparticles and the displacements of these nanoparticles between time points.

Further details are given in *SI Appendix*. This includes a detailed schematic of the freezing apparatus, the protocol for growing large crystals of ice in the cell, and a description of the technique for estimating the orientation of ice crystals. *SI Appendix* also describes how we measure temperature gradients in the cell and the precise calculation details involved in TFM. Finally, we provide a derivation of Eq. **1**.

Data Availability. All study data are included in the article and/or *SI Appendix*.

ACKNOWLEDGMENTS. This research was supported by Eidgenössche Technische Hochschule Research Grant ETH-38 18-2. We thank John Wettlaufer, Alan Rempel, Ian Griffiths and Tongxin Zhang for helpful discussions.

1. J. G. Dash, A. W. Rempel, J. S. Wettlaufer, The physics of premelted ice and its geophysical consequences. *Rev. Mod. Phys.* **78**, 695–741 (2006).
2. R. W. Style, M. G. Worster, Surface transport in premelted films with application to grain-boundary grooving. *Phys. Rev. Lett.* **95**, 176102 (2005).
3. L. A. Wilen, J. S. Wettlaufer, M. Elbaum, M. Schick, Dispersion-force effects in interfacial premelting of ice. *Phys. Rev. B Condens. Matter* **52**, 12426–12433 (1995).
4. D. N. Sibley, P. Llombart, E. G. Noya, A. J. Archer, L. G. MacDowell, How ice grows from premelting films and water droplets. *Nat. Commun.* **12**, 239 (2021).
5. V. Sadtchenko, G. E. Ewing, Interfacial melting of thin ice films: An infrared study. *J. Chem. Phys.* **116**, 4686–4697 (2002).
6. Y. Furukawa, M. Yamamoto, T. Kuroda, Ellipsometric study of the transition layer on the surface of an ice crystal. *J. Cryst. Growth* **82**, 665–677 (1987).
7. K. I. Murata, H. Asakawa, K. Nagashima, Y. Furukawa, G. Sazaki, Thermodynamic origin of surface melting on ice crystals. *Proc. Natl. Acad. Sci. U.S.A.* **113**, E6741–E6748 (2016).
8. S. Tyagi, H. Huynh, C. Monteux, S. Deville, Objects interacting with solidification fronts: Thermal and solute effects. *Materialia (Oxf.)* **12**, 100802 (2020).
9. J. S. Wettlaufer, M. G. Worster, Premelting dynamics. *Annu. Rev. Fluid Mech.* **38**, 427–452 (2006).
10. J. M. H. Schollick *et al.*, Segregated ice growth in a suspension of colloidal particles. *J. Phys. Chem. B* **120**, 3941–3949 (2016).
11. K. G. Libbrecht, Physical dynamics of ice crystal growth. *Annu. Rev. Mater. Res.* **47**, 271–295 (2017).
12. B. V. Derjaguin, N. V. Churaev, Flow of nonfreezing water interlayers and frost heaving. *Cold Reg. Sci. Technol.* **12**, 57–66 (1986).
13. S. Kjelstrup, S. A. Ghoreishian Amiri, B. Loranger, H. Gao, G. Grimstad, Transport coefficients and pressure conditions for growth of ice lens in frozen soil. *Acta Geotech.* **16**, 2231–2239 (2021).
14. R. R. Gilpin, A model for the prediction of ice lensing and frost heave in soils. *Water Resour. Res.* **16**, 918–930 (1980).
15. J. S. Wettlaufer, M. G. Worster, L. A. Wilen, J. G. Dash, A theory of premelting dynamics for all power law forces. *Phys. Rev. Lett.* **76**, 3602–3605 (1996).
16. I. Vlahou, M. G. Worster, Freeze fracturing of elastic porous media: A mathematical model. *Proc Math Phys Eng Sci* **471**, 20140741 (2015).
17. J. S. Wettlaufer, M. G. Worster, Dynamics of premelted films: Frost heave in a capillary. *Phys. Rev. E Stat. Phys. Plasmas Fluids Relat. Interdiscip. Topics* **51**, 4679–4689 (1995).
18. L. Gagliardi, O. Pierre-Louis, The nonequilibrium crystallization force. *EPL* **127**, 7 (2019).
19. A. W. Rempel, Microscopic and environmental controls on the spacing and thickness of segregated ice lenses. *Quat. Res.* **75**, 316–324 (2011).
20. S. S. L. Peppin, R. W. Style, The physics of frost heave and ice-lens growth. *Vadose Zone J.* **12**, 1–12 (2013).
21. R. W. Style, S. S. L. Peppin, The kinetics of ice-lens growth in porous media. *J. Fluid Mech.* **692**, 482–498 (2012).
22. J. M. Konrad, N. R. Morgenstern, A mechanistic theory of ice lens formation in fine-grained soils. *Can. Geotech. J.* **17**, 473–486 (1980).
23. S. A. Ketcham, P. B. Black, R. Pretto, Frost heave loading of constrained footing by centrifuge modeling. *J. Geotech. Geoenviron. Eng.* **123**, 874–880 (1997).
24. J. J. Beaudoin, C. MacInnis, The mechanism of frost damage in hardened cement paste. *Cement Concr. Res.* **4**, 139–147 (1974).
25. J. You *et al.*, In situ observation of the unstable lens growth in freezing colloidal suspensions. *Colloids Surf. A Physicochem. Eng. Asp.* **553**, 681–688 (2018).
26. K. Watanabe, M. Mizoguchi, Amount of unfrozen water in frozen porous media saturated with solution. *Cold Reg. Sci. Technol.* **34**, 103–110 (2002).
27. H. Ozawa, S. Kinosita, Segregated ice growth on a microporous filter. *J. Colloid Interface Sci.* **132**, 113–124 (1989).
28. J. M. Konrad, Influence of freezing mode on frost heave characteristics. *Cold Reg. Sci. Technol.* **15**, 161–175 (1988).
29. J. Zhou, C. Wei, Ice lens induced interfacial hydraulic resistance in frost heave. *Cold Reg. Sci. Technol.* **171**, 102964 (2020).
30. M. Vignes, K. M. Dijkema, A model for the freezing of water in a dispersed medium. *J. Colloid Interface Sci.* **49**, 165–172 (1974).
31. L. A. Wilen, J. G. Dash, Frost heave dynamics at a single crystal interface. *Phys. Rev. Lett.* **74**, 5076–5079 (1995).
32. D. Dedovets, C. Monteux, S. Deville, A temperature-controlled stage for laser scanning confocal microscopy and case studies in materials science. *Ultramicroscopy* **195**, 1–11 (2018).
33. R. W. Style *et al.*, Liquid-liquid phase separation in an elastic network. *Phys. Rev. X* **8**, 011028 (2018).
34. J. Y. Kim *et al.*, Extreme cavity expansion in soft solids: Damage without fracture. *Sci. Adv.* **6**, eaaz0418 (2020).
35. P. D. Garcia, R. Garcia, Determination of the elastic moduli of a single cell cultured on a rigid support by force microscopy. *Biophys. J.* **114**, 2923–2932 (2018).
36. R. W. Style *et al.*, Traction force microscopy in physics and biology. *Soft Matter* **10**, 4047–4055 (2014).
37. S. Hell, G. Reiner, C. Cremer, E. H. K. Stelzer, Aberrations in confocal fluorescence microscopy induced by mismatches in refractive index. *J. Microsc.* **169**, 391–405 (1993).
38. T. H. Besseling, J. Jose, A. Van Blaaderen, Methods to calibrate and scale axial distances in confocal microscopy as a function of refractive index. *J. Microsc.* **257**, 142–150 (2015).
39. W. Knoche, "Chemical reactions of CO_2 in water" in *Biophysics and Physiology of Carbon Dioxide*, C. Bauer, G. Gros, H. Bartels, Eds. (Springer, Berlin, Germany, 1980), pp. 3–11.
40. T. Zhang, Z. Wang, L. Wang, J. Li, J. Wang, Quantitative determination of tip undercooling of faceted sea ice with in situ experiments. *J. Phys. Condens. Matter* **33**, 36LT01 (2021).
41. T. Zhang, L. Wang, Z. Wang, J. Li, J. Wang, Single ice crystal growth with controlled orientation during directional freezing. *J. Phys. Chem. B* **125**, 970–979 (2021).
42. F. D. Bloss, *Optical Crystallography* (MSA Monograph Series, Mineralogical Society of America, Washington, DC, 1999).
43. M. Bauer, GitHub/calculated_Michel_Levy_Chart (2019). https://github.com/markus-bauer/calculated_Michel_Levy_Chart. Accessed 14 January 2022.
44. B. E. Sørensen, A revised Michel-Lévy interference colour chart based on first-principles calculations. *Eur. J. Mineral.* **25**, 5–10 (2013).
45. L. A. Wilen, C. L. Diprinzio, R. B. Alley, N. Azuma, Development, principles, and applications of automated ice fabric analyzers. *Microsc. Res. Tech.* **62**, 2–18 (2003).
46. B. Sabass, M. L. Gardel, C. M. Waterman, U. S. Schwarz, High resolution traction force microscopy based on experimental and computational advances. *Biophys. J.* **94**, 207–220 (2008).
47. Y. Xu *et al.*, Imaging in-plane and normal stresses near an interface crack using traction force microscopy. *Proc. Natl. Acad. Sci. U.S.A.* **107**, 14964–14967 (2010).
48. B. Slater, A. Michaelides, Surface premelting of water ice. *Nat. Rev. Chem.* **3**, 172–188 (2019).

49. H. Dosch, A. Lied, J. H. Bilgram, Glancing-angle X-ray scattering studies of the premelting of ice surfaces. *Surf. Sci.* **327**, 145–164 (1995).
50. P. Bian, Y. Wang, T. J. McCarthy, Rediscovering silicones: The anomalous water permeability of "hydrophobic" pdms suggests nanostructure and applications in water purification and anti-icing. *Macromol. Rapid Commun.* **42**, e2000682 (2021).
51. L. A. Wilen, J. G. Dash, Giant facets at ice grain boundary grooves. *Science* **270**, 1184–1186 (1995).
52. A. W. Rempel, C. R. Meyer, Premelting increases the rate of regelation by an order of magnitude. *J. Glaciol.* **65**, 518–521 (2019).
53. D. Nenow, A. Trayanov, Surface premelting phenomena. *Surf. Sci.* **213**, 488–501 (1989).
54. J. Hickman, Y. Mishin, Disjoining potential and grain boundary premelting in binary alloys. *Phys. Rev. B* **93**, 224108 (2016).
55. K. A. Rosowski *et al.*, Elastic ripening and inhibition of liquid-liquid phase separation. *Nat. Phys.* **16**, 422–425 (2020).
56. K. Sekine, A. Okamoto, K. Hayashi, In situ observation of the crystallization pressure induced by halite crystal growth in a microfluidic channel. *Am. Mineral.* **96**, 1012–1019 (2011).
57. L. A. Rijniers, H. P. Huinink, L. Pel, K. Kopinga, Experimental evidence of crystallization pressure inside porous media. *Phys. Rev. Lett.* **94**, 075503 (2005).
58. J. Desarnaud, D. Bonn, N. Shahidzadeh, The pressure induced by salt crystallization in confinement. *Sci. Rep.* **6**, 30856 (2016).
59. R. J. Flatt, F. Caruso, A. M. A. Sanchez, G. W. Scherer, Chemo-mechanics of salt damage in stone. *Nat. Commun.* **5**, 4823 (2014).
60. D. V. Wiltschko, J. W. Morse, Crystallization pressure versus "crack seal" as the mechanism for banded veins. *Geology* **29**, 79–82 (2001).
61. M. G. Worster, Convection in mushy layers. *Annu. Rev. Fluid Mech.* **29**, 91–122 (1997).
62. J. S. Wettlaufer, Impurity effects in the premelting of ice. *Phys. Rev. Lett.* **82**, 2516–2519 (1999).